Combustion Science and Technology

ISSN: (Print) (Online) Journal homepage: https://www.tandfonline.com/loi/gcst20

Influence of Rare-Earth Promoters (Ce, Zr and La) on Catalytic Performance of Copper-Based Catalyst in Toluene Oxidation

Guangtao Hu, Zirui Zhang, Chang'an Wang, Guojie Li, Dandan Zhou, Jinshi Wang, Defu Che & Running Kang

To cite this article: Guangtao Hu, Zirui Zhang, Chang'an Wang, Guojie Li, Dandan Zhou, Jinshi Wang, Defu Che & Running Kang (26 Nov 2023): Influence of Rare-Earth Promoters (Ce, Zr and La) on Catalytic Performance of Copper-Based Catalyst in Toluene Oxidation, Combustion Science and Technology, DOI: 10.1080/00102202.2023.2288671

To link to this article: https://doi.org/10.1080/00102202.2023.2288671

COMBUSTION SCIENCE AND TECHNOLOGY
https://doi.org/10.1080/00102202.2023.2288671

Influence of Rare-Earth Promoters (Ce, Zr and La) on Catalytic Performance of Copper-Based Catalyst in Toluene Oxidation

Guangtao Hu[a,b], Zirui Zhang[c], Chang'an Wang[a], Guojie Li[b], Dandan Zhou[b], Jinshi Wang[a,b], Defu Che[a], and Running Kang[c]

[a]School of Energy and Power Engineering, Xi'an Jiaotong University, Xi'an, PR China; [b]School of Energy Engineering, Yulin University, Yulin, PR China; [c]State Key Laboratory of High-Temperature Gas Dynamics, Institute of Mechanics, Chinese Academy of Sciences, Beijing, PR China

ABSTRACT

Copper-infused mixed metal oxides have been identified as powerful catalysts for eliminating volatile organic compounds (VOCs) due to their widespread availability and cost-effectiveness. The copper metal oxide catalysts were synthesized using the sol-gel method and promoted with rare earth elements, La, Ce, and Zr, to catalyze the oxidation of toluene. Compared to all tested catalysts, $CuLaO_x$ demonstrates the least activity igniting activity even though La appears to enhance copper dispersion and generate a large number of oxygen species on the surface. $CuZrO_x$ displays remarkable thermal stability, resulting in a minimal amount of lattice oxygen participating in toluene oxidation. The introduction of Ce into the $CuCeO_x$ catalyst enhances its activity significantly, attributed to the exceptional reducibility of copper species. Therefore, the TOF for the $CuCeO_x$, $CuLaO_x$ and $CuZrO_x$ catalysts are $9.23–24.8 \times 10^{-3}$ s^{-1}, $1.29–6.22 \times 10^{-3}$ s^{-1}, and $1.05–10.03 \times 10^{-3}$ s^{-1} at 200–400 °C, respectively. The infrared spectra, observed at varying temperatures during toluene oxidation, were presented. Interestingly, all catalysts demonstrated a comparable reaction pathway. The catalytic oxidation mechanism is expected to proceed via the intermediates of toluene-alkoxide-aldehydic-carboxylic acid, ultimately culminating in complete degradation to CO_2 and H_2O. This study establishes a theoretical foundation for the judicious selection of suitable rare earth elements as promoters, enabling the development of copper-based catalysts for efficient volatile organic compound (VOC) removal in industrial settings.

ARTICLE HISTORY
Received 27 September 2023
Revised 8 November 2023
Accepted 23 November 2023

KEYWORDS
Copper; rare-earth; VOCs oxidation; toluene; IR spectra

Introduction

Volatile organic compounds (VOCs) are organic chemicals that have a low boiling point (<250°C) at standard atmospheric pressure. This group includes benzene, toluene, and xylene, among others, which pose significant threats to both the environment and public well-being. The potential health risks associated with prolonged exposure to VOCs are substantial, with many of these compounds being linked to respiratory illnesses, and even the development of cancer and genetic mutations over extended periods of contact (Deng et al. 2023; Gao et al. 2023; Wang et al. 2017). In recent times, an increasing body of research

CONTACT Defu Che dfche@mail.xjtu.edu.cn School of Energy Engineering, Yulin University, Yulin, PR Chinal; Running Kang kangrunning@imech.ac.cn State Key Laboratory of High-Temperature Gas Dynamics, Institute of Mechanics, Chinese Academy of Sciences, Beijing, PR China
Supplemental data for this article can be accessed online at https://doi.org/10.1080/00102202.2023.2288671

has been directed toward catalytic oxidation as a prominent approach. This method is recognized for its high efficiency, minimal energy consumption, and environmentally friendly attributes. It offers a robust means of transforming volatile organic compound molecules into innocuous water (H_2O) and carbon dioxide (CO_2), ensuring comprehensive and safe conversion (Guo et al. 2019). Consequently, a variety of materials, including noble metal catalysts supported and catalysts of transition metal oxides, have been utilized to tackle the removal of VOCs. Noble metal catalysts have been widely acknowledged for their efficacy in VOCs abatement, showcasing commendable catalytic activity at lower temperatures. However, their considerable expense has posed a significant impediment to their widespread adoption in industrial applications (Liu et al. 2018, Hu, Li, and Liu 2018. Hence, transition metal oxides catalysts, recognized as a promising and viable alternative, have emerged as popular selections. Their appeal lies in advantageous attributes, including cost-effectiveness and robust catalytic performance, particularly at reduced temperatures (Brummer et al. 2022).

Numerous literature sources highlight the extensive utilization of copper oxides, primarily owing to the distinctive attributes of the Cu(II)/Cu(I) redox pair, which renders a multitude of their complexes well-suited for diverse environmentally friendly catalytic reactions. There are synthesized zeolite-like materials from coal fly ash modified by copper that directed to economical degradation of VOCs molecules, such as hexane, acetone, toluene, 1,2 dichlorobenzene etc. with different functionality (Boycheva et al. 2019. It provided evidence that the formaldehyde thermos-catalytic oxidation was performed mainly according to Mars-van Krevelen mechanism (Qiang et al. 2022). This process involves oxidizing formaldehyde molecules with lattice oxygen, and then re-oxidizing the copper oxides into copper oxides with gas phase oxygen after the formaldehyde molecules are oxidized. As noted by Paul (Paul et al. 2022), a subset of Cu(II) compounds within the broader category of bulk copper oxides has been employed in toluene oxidation, yielding up to 11%. It is apparent that the observed low activity and limited product yield represent significant challenges warranting immediate attention. Consequently, there is a compelling impetus to address these concerns by investigating the catalytic reaction through the utilization of multi-metal combinations.

The enhancement of transition metal oxide catalysts' catalytic activity can be achieved by two distinct strategies, namely elemental doping and structural modification (Hu, Li, and Liu 2018)In the context of dopant incorporation, a noticeable modulation of surface electronic properties can be achieved by altering the donor-acceptor interactions between the substrate and dopant elements. This in turn helps to improve the capacity of the redox catalytic converter. It substantiated that effective dispersion of copper on a cerium-based support results in a Cu-O-Ce structure, which yields heightened availability of activated oxygen through oxygen vacancies and confers enhanced resilience against catalytic deactivation (Ye et al. 2023. In another study, Cu-Mn mixed oxides were synthesized with diverse Cu/Mn molar ratios, revealing that the $Cu_1Mn_1O_x$ specimen displayed superior efficacy in toluene removal, sustaining its activity at 214°C over a span of 120 hours without substantial deactivation (Hu, Li, and Liu 2018). An alternate approach, referred to as structure modification, involves the adjustment of surface physicochemical properties to enhance combustion efficiency. For instance, the interaction between copper and ceria undergoes significant alteration upon deposition onto SBA-15 mesoporous silica. This modification controls the manner in which metal oxide particles are loaded, regulated by their dispersion

and positioning within the porous structure (Tsoncheva et al. 2013). It has been extensively examined whether rare-earth promoters, such as Ce, Zr, and La, can be incorporated into catalysts made from metals such as Cu, Mn, Co, and Ni for their ability to influence metallic particle size and distribution, thereby impacting their catalytic performance. This phenomenon is observable across various catalytic reactions, encompassing steam reforming (Sepehri and Rezaei 2015, Aasberg-Petersen et al. 2011, Vizcaíno, Carrero, and Calles 2012, Fischer – Tropsch synthesis (Hong et al. 2010, Zhang; Zhang et al. 2012), methanol decomposition (Mu et al. 2008) and benzene oxidation (Mu et al. 2010, among others. In particular, La_2O_3 serves a dual role within catalytic systems. It not only prevents the undesirable sintering of metal particles, but it also possesses the unique capability to cleanse the catalyst surface from carbonaceous deposits. This cleansing ability arises from the existence of oxycarbonate species, particularly $La_2O_2CO_3$, which reacts well with carbon deposits, resulting in the release of CO and the regeneration of the La_2O_3 phase (Arandiyan et al. 2014; Srinivas et al. 2003). Within the catalytic matrix, CeO_2 plays a pivotal role, showcasing exceptional proficiency in both storing and releasing oxygen. This distinctive characteristic contributes to low-temperature catalytic activity, a crucial feature for numerous catalytic reactions. Ceria (CeO_2) manifests two discernible oxygen species, namely surface-bound oxygen and bulk oxygen, both of which contribute significantly to its oxygen storage capacity (Cheng et al. 1996; Doukkali et al. 2012). Moreover, the incorporation of isovalent cations, such as zirconium (Zr), into the active metal framework enhances the overall oxygen storage capacity. This improvement stems from the generation of external oxygen vacancies, which in turn bolster the mobility of oxygen entities. It's noteworthy, however, that the bulk oxygen mobility remains notably lower compared to the oxygen mobility observed at the surface of the catalyst (Reddy, Katta, and Thrimurthulu 2010). However, many results so far were only related to the few of rare-earth promoters for catalytic reaction. The comparison of the interaction effect between different rare-earth promoters and copper is necessary, which is beneficial for further study and better exploring the nature of the interaction property.

To investigate the influence of rare-earth promoters La_2O_3, CeO_2, and ZrO_2 on the interaction with copper oxides in catalyzing the elimination of VOCs, this current study undertook the synthesis of La-, Ce-, and Zr-facilitated copper metal oxide catalysts through the sol-gel method. These catalysts were subsequently evaluated for their performance in toluene oxidation. Toluene was chosen as the probe molecule for activity assessments due to its frequent occurrence in industrial emissions and its substantial contribution to photochemical ozone formation potential (Piumetti, Fino, and Russo 2015). The analysis that followed involved a thorough examination of the structural and surface characteristics of the synthesized catalysts, using a range of physical-chemical techniques. These techniques were diverse and complementary in nature. Furthermore, a detailed mechanistic framework for the process of toluene oxidation over these materials was meticulously formulated and is presented herein.

Experimental

Catalyst preparation

The $CuLaO_x$, $CuCeO_x$, and $CuZrO_x$ catalysts were synthesized via the sol-gel method using $Cu(NO_3)_2{\cdot}3\,H_2O$, $La(NO_3)_3{\cdot}6\,H_2O$, $Ce(NO_3)_3{\cdot}6\,H_2O$, and $Zr(NO_3)_4{\cdot}5\,H_2O$ precursors. In

the synthesis of $CuCeO_x$, a solution consisting of $Cu(NO_3)_2 \cdot 3\ H_2O$ and $Ce(NO_3)_3 \cdot 6\ H_2O$ in a molar ratio of 1:1 molar ratio was dissolved fully in 140 mL of ethanol at 80°C. Concurrently, a solution containing oxalic acid (0.24 mol/L), acting as a pore-forming agent, was rapidly introduced into the aforementioned nitrate solution under continuous stirring. This process facilitated both ethanol evaporation and complete dissolution of all constituents, resulting in the formation of a gel matrix. The gel synthesis was conducted at 80°C for a duration of approximately 6 hours. Subsequent to this, the gel underwent an aging process at ambient temperature for a duration of 48 hours, after which it was subjected to a drying phase at 105°C for a span of 12 hours. Subsequently, the gel underwent calcination in an ambient air environment at 550°C for a period of 2 hours. The synthesis protocol was consistently applied to $CuLaO_x$ and $CuZrO_x$ catalysts, enabling a comprehensive comparative assessment of the distinct effects associated with various copper oxide compositions.

Characterization

The identification of crystalline phases was conducted using the PERSEE XD-3 automated diffractometer, which is capable of powder X-ray diffraction (XRD). Utilizing Cu Kα radiation (40 kV, 200 mA, $\lambda = 1.5418$ Å) as the X-ray source, data were garnered in a 2θ range between 5 and 80°, with an incremental scanning step of 0.02°. To explore the electronic structure and surface chemistry, we conducted X-ray photoelectron spectroscopy (XPS) measurements with the Kratos Axis Ultra DLD spectrometer. This instrument used a monochromatic Al-Kα X-ray source and a delay line detector. The binding energies were calibrated by referencing the C 1s peak (284.8 eV), which was derived from adventitious carbon. To investigate the hydrogen reduction behavior, we carried out the Temperature Programmed Reduction (H_2-TPR) analysis using the TP-5080B Auto multifunctional adsorption apparatus, fitted with a thermal conductivity detector (TCD). Before conducting H_2-TPR and Oxygen Programmed Desorption (O_2-TPD) experiments, each 20 mg sample underwent a heating process at 500°C for 30 minutes in a pure Ar atmosphere (flowing at 30 mL/min). During the H_2-TPR experiments, the specimen underwent reduction in a 5% H_2/Ar environment (30 mL/min), where the temperature was progressively raised from ambient to 600°C at a pace of 10°C/min. Meanwhile, in O_2-TPD experiments, sample exposed to O_2 for 1 hour at room temperature followed by an Ar purge for 0.5 hours (30 mL/min). Subsequently, the reactor temperature was raised stepwise to 950°C, increasing at a rate of 10°C/min. In situ infrared (IR) studies were performed using the Bruker Tensor 27 apparatus, integrated with a specially designed magnetically-driven transmission cell. Approximately 5 mg of the catalyst was mixed with 50 mg of KBr and then compacted into a standalone wafer. After stabilization within a quartz IR cell, the catalyst was subjected to an argon (Ar) flow at 300°C for 1 hour. The initial IR spectrum was recorded at room temperature for reference. Subsequently, the gas flow was switched to either 500 ppm C_7H_8 in N_2 or a mixture of 500 ppm C_7H_8 and 21% O_2 in N_2. Exposure continued for 0.5 hours until saturation was reached. The experiment involved nitrogen desorption and a continuous flow reaction process, with the temperature increasing from room temperature to 400°C at a rate of 10°C/min. At every temperature increment, a sequence of temporally-resolved IR spectra, documenting the reaction on the specimen, was chronologically acquired with a resolution of 4 cm^{-1}, encompassing a total of 64 scans.

Catalytic activity test

The assessment of catalytic activity, known as temperature programmed oxidation (TPO), was conducted under ambient pressure using a specifically designed continuous-flow setup. This equipment featured a micro-reactor with a 4 mm internal diameter, ensuring a regulated setting for the assessment. In this experimentation, a representative sample of 200 mg was compacted into sheets and subsequently sieved to achieve a mesh size ranging from 20 to 40. The resulting sieved material was then carefully introduced into the reactor. A composite gas stream composed of 500 ppm C_7H_8 and 21% O_2 in a nitrogen (N_2) carrier gas was introduced into the reactor. For consistent testing conditions, we maintained a steady overall flow rate of 300 mL/min, resulting in a gas hourly space velocity (GHSV) of 40,000 h^{-1}. To precisely monitor the self-sustaining combustion of the catalyst, a dual set of K-type thermocouples with a diameter of 0.5 mm were strategically employed. The initial thermocouple was strategically placed at the catalyst bed center to enable continuous temperature monitoring. Simultaneously, the second thermocouple was positioned between the oven wall and reactor wall to achieve accurate control of oven temperature. To characterize the behavior of the catalyst during temperature programmed oxidation (TPO), we meticulously applied a consistent heating rate of 10°C/min. Throughout each TPO run, the evolving effluent gases, including C_7H_8, O_2, and CO_2, were meticulously and continuously monitored. This was achieved through the utilization of an online mass spectrometer (Omistar, Pfeiffer), ensuring real-time tracking of the gas composition and aiding in the comprehensive analysis of the catalytic reactions taking place within the system.

Results and discussion

Catalysts structure and composition

Figure 1 shows the XRD patterns illustrating the crystalline composition of each catalyst. Notable characteristic peaks associated with bulk CuO are evident at 2θ values of 32.5°, 35.7°, 38.7°, 48.8°, 53.5°, 58.4°, 61.7°, 66.2°, and 68.2°, which correspond to (110), (002), (111), (202), (020), (202), (113), (022), and (220) reflection planes, respectively (Kanchana et al. 2023. These peak positions are in accordance with the JCPDS card number 45–0937, which pertains to CuO nanoparticles. For ceria, the XRD pattern predominantly exhibits anticipated lines corresponding to fluorite CeO_2 (JCPDS: 43–1002). Peaks representing crystalline ceria are apparent at 2θ values of 28.6°, 33.1°, 47.5°, and 56.3°, denoting the (111), (200), (220), and (311) planes, respectively (Kang et al. 2021). In the XRD pattern of $CuCeO_x$, discernible low diffraction peaks are present. This signifies enhanced dispersion or reduced crystalline particle sizes of copper and cerium species within $CuCeO_x$, attributed to the formation of a Cu-Ce solid solution. Also, the above characteristic peaks about CeO_2 for the $CuCeO_x$ are weakened and broadened, indicating that well dispersed particle sizes of CuO (6.2 nm calculated by Scherrer Equation) and CeO_2 can improve the catalytic activity of $CuCeO_x$ compared to those of the bulk CuO. With respect to $CuZrO_x$, the absence of any distinguished peaks for the zirconium species in the pattern confirms the amorphous forms to ZrO_2. Nonetheless, the presence of CuO phases is still possible, particularly since the molar ratio of copper to zirconium in the solids is close to the critical value (Cu/Zr = 1), which corresponds to CuO particle sizes of 7.1 nm. No obvious phase related to copper

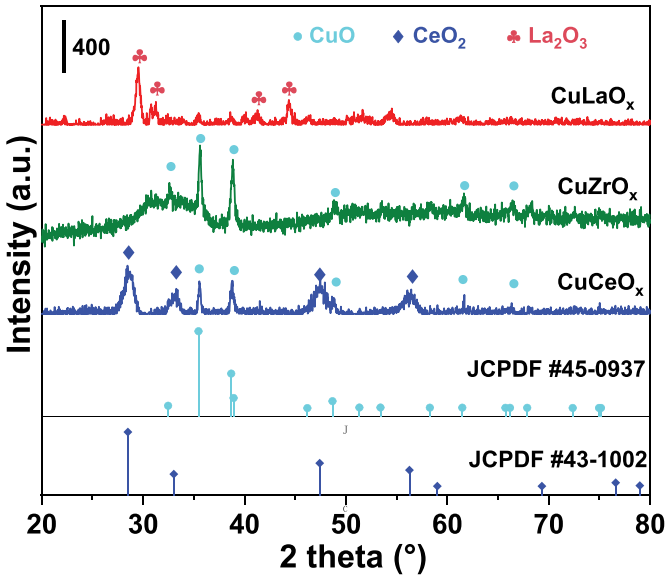

Figure 1. XRD patterns of the calcined $CuCeO_x$, $CuZrO_x$ and $CuLaO_x$ catalysts.

compounds is found for the $CuLaO_x$, and only faint lanthanum compound can be detected. Both copper and lanthanum can aid in the formation of a solid solution, in which the copper or lanthanum compounds appear as either amorphous phases or extremely small particles that are difficult to detect with X-ray diffraction.

Elemental conditions were analyzed within the catalysts using XPS. The relevant narrow spectra are illustrated in Figure 2, and the surface compositions of the primary elements are detailed in Table 1. A review of the Cu 2p spectra for each catalyst presented in Figure 2a shows two distinct peaks. The peak around 933 eV corresponds to Cu $2p_{3/2}$, while the peak located at approximately 953 eV corresponds to Cu $2p_{1/2}$. Remarkably, discernible satellite peaks within the energy range of 940 eV to 944 eV and 962 eV, indicative of characteristic Cu^{2+} oxidation state features, are observed. The Cu $2p_{3/2}$ peaks exhibit noticeable asymmetry. Through rigorous analysis and modeling of the experimental data, it is discerned that the Cu $2p_{3/2}$ peak can be effectively modeled by two distinct peaks positioned at 932.9 and 934.7 eV, which correspond to Cu^{+} and Cu^{2+} ions, respectively (Bin et al. 2015 Given the XPS probing depth of about 3–10 nm, the abundant presence of Cu^{2+} species on the catalyst's surface notably facilitates the provision of lattice oxygen, thereby enabling enhanced adsorption and the comprehensive oxidation of toluene (Zhang et al. 2023. With regard to the XPS spectra of Ce 3d in the $CuCeO_x$ catalysts, detailed deconvolution has been carried out, leading to the resolution of eight discernible peaks (Figure 3b). These peaks correspond to the $3d_{5/2}$ and $3d_{3/2}$ spin-orbit components, labeled as v and u, respectively, which represent the electronic shifts between $Ce^{4+} \leftrightarrow Ce^{3+}$. Peaks labeled as v′ (885.6 eV) and u′ (903.4 eV) signify the characteristic features of Ce^{3+}. Meanwhile, the peaks v (882.6 eV), v″ (889.6 eV), v‴ (898.5 eV), u (901.1 eV), u″ (907.9 eV), and u‴ (916.9 eV) indicate the unique imprints of Ce^{4+}. This observation substantiates the coexistence of both Ce^{3+} and Ce^{4+} species within the catalysts, accompanied by the presence of an imperfect structure $[Ce_{1-\sigma}{}^{4+}Ce_{\sigma}{}^{3+}]$ $[O_{2-\sigma/2}O_{\sigma/2}]$ on the surface of CeO_2 (Liu et al. 2021;

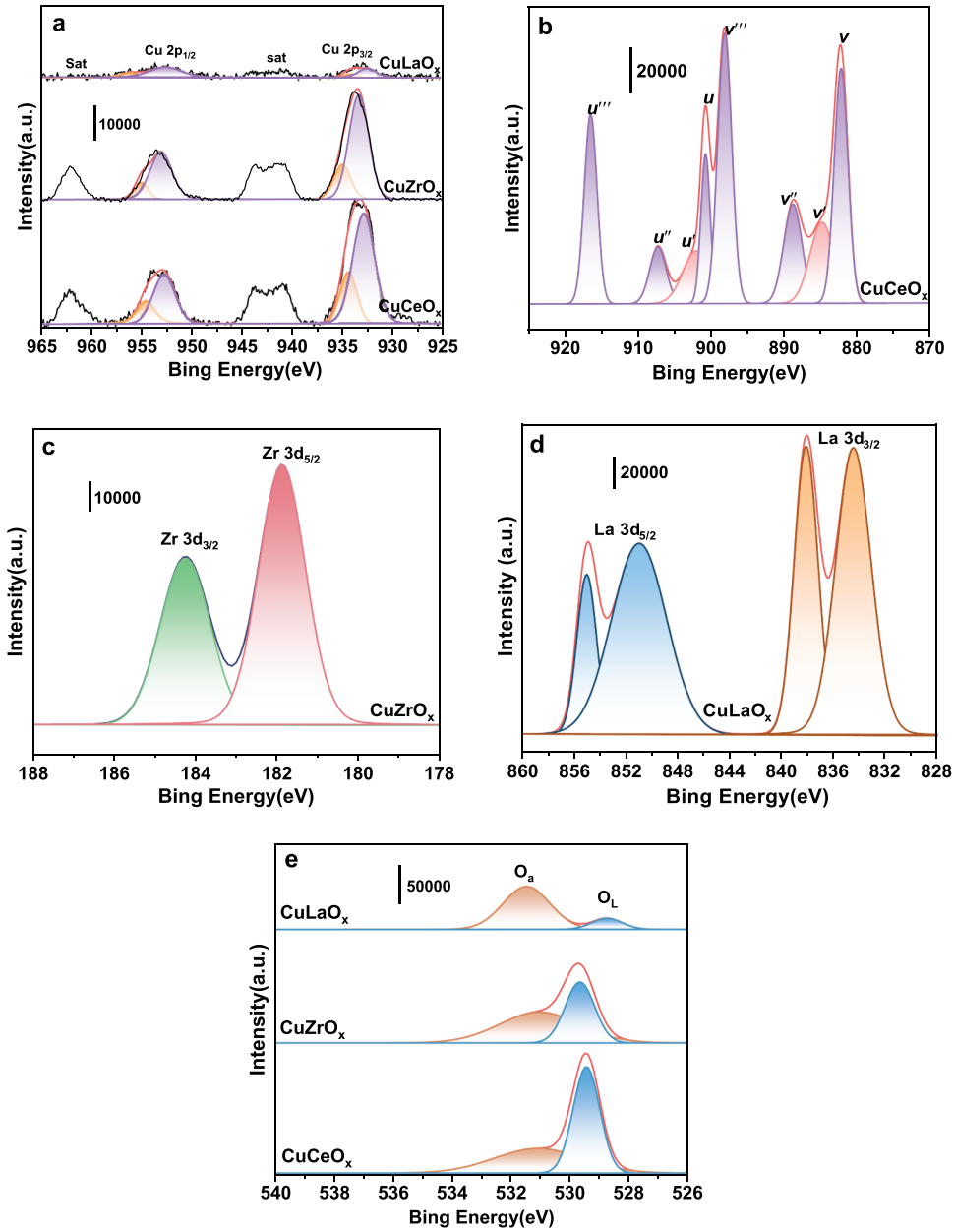

Figure 2. XPS narrow spectra of cu 2p (a), ce 3d (b), zr 3d (c), La 3d (d) and O 1s (e) of the $CuMO_x$ (*M* = ce, zr, La) catalysts.

Yun et al. 2022). The presence of Ce^{3+} is widely acknowledged to be linked to the generation of oxygen vacancies, which in turn contributes to the Ce^{3+}/Ce^{4+} redox pairing. The calculated ratio of 0.37, derived from the total area of the Ce^{3+} peaks relative to the Ce^{4+} region, signifies the presence of mobile oxygen species and oxygen vacancies, which substantively augment the catalytic performance. Moving to the Zr 3d spectra observed in $CuZrO_x$, shown in Figure 2c, clear doublets representing Zr $3d_{3/2}$ at about 184.5 eV and Zr

Table 1. Surface compositions $CuCeO_x$, $CuZrO_x$ and $CuLaO_x$ derived from XPS analysis.

	Surface element composition (at%)							
Catalyst	Cu	Ce	Zr	La	O	Cu/O	$Cu^+/(Cu^{2+}+Cu^+)$	$O_a/(O_L+O_a)$
$CuCeO_x$	15.76	16.55	–	–	67.69	0.23	0.75	0.63
$CuZrO_x$	4.15	–	4.08	–	91.77	0.04	0.49	0.54
$CuLaO_x$	2.44	–	–	22.18	75.38	0.03	0.41	0.53

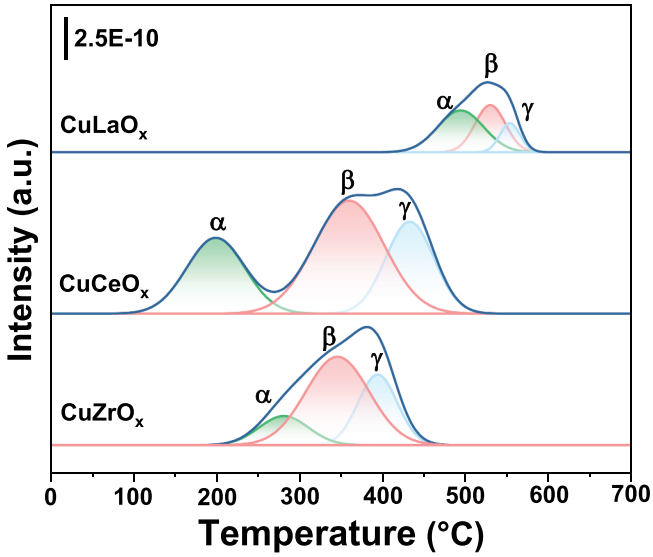

Figure 3. H_2-TPR profiles of $CuCeO_x$, $CuZrO_x$ and $CuLaO_x$ catalysts. Weight of catalyst: 20 mg; pretreatment: pure ar at 500°C for 30 min; measurement conditions: 5% H_2/Ar (30 mL/min), heating rate 10°C/min from 50–800°C.

$3d_{5/2}$ at approximately 182.1 eV are apparent. Notably, the binding energy of Zr $3d_{5/2}$ in $CuZrO_x$ is observed to be slightly lower than that of pure ZrO_2 (at 182.4 eV), yet higher than that of zirconium metal (at 180.0 eV). This phenomenon is attributed to robust Cu-Zr interactions, engendering the charge transfer from copper to zirconium. The existence of more reduced zirconium species can also be linked to a higher density of oxygen vacancies within the ZrO_2 lattice (Jones et al. 2010). Furthermore, the occurrence of zirconium cations with lower binding energies in comparison to bulk ZrO_2 can be attributed to the proximity of copper oxides to the oxygen vacancies embedded within the ZrO_2 matrix (Wang et al. 2007). Figure 2d depicts the La 3d core-level X-ray photoelectron spectra of the catalysts, illustrating characteristic patterns consistent with La^{3+} compounds (Dudric et al. 2014, Wang et al. 2018. The observed dual peaks arise from the spin-orbit interaction, leading to the separation of the $3d_{5/2}$ and $3d_{3/2}$ lines. Furthermore, each molecule undergoes additional splitting caused by the electron shift from the oxygen ligands to the La 4f orbitals, resulting in the emergence of peaks located at 833.2, 837.6, 850.1, and 854.5 eV, respectively. This separation of the $3d_{5/2}$ and $3d_{3/2}$ spin-orbit transitions of La^{3+} ions, coupled with the interplay between nuclear holes and electrons transferring from the O 2p valence band to the vacant La 4f orbitals, gives rise to the distinct double-peak pattern discernible in the La 3d core-level X-ray photoelectron spectra. The XPS peaks corresponding to O 1s exhibit

asymmetry, prompting a meticulous deconvolution procedure aimed at discerning the relative content of various oxygen species based on their distinct low and high binding energies. This thorough analysis is enabled through precise curve-fitting methodologies, as depicted in Figure 2e. Within the spectral range of 529.0–529.7 eV, the peak is attributed to regular lattice oxygen (O_L), emblematic of the metal-oxygen bonds intrinsic to the crystalline lattice. Conversely, the peak positioned at 531.5 eV is ascribed to surface chemisorbed oxygen species (O_a), encompassing entities such as O^-, O^{2-}, and O_2^{2-}. The quantitative elemental compositions were deduced from the areas under the Cu 2p, Ce 3d, Zr 3d, La 3d, and O 1s peaks, as exhaustively documented in Table 1. Importantly, XPS operates as a surface-sensitive technique that predominantly captures species present on the sample's surface. The results support that the copper content on the surface is lower than the oxygen content, as shown by the Cu/O equivalent ratio of 0.42. Of particular significance is the notably higher Cu/O ratio exhibited by $CuCeO_x$ in comparison to $CuZrO_x$ and $CuLaO_x$. During the catalytic combustion process, a critical stage involves the adsorption and activation of toluene molecules at copper sites (Zhao et al. 2019). To quantitatively gauge this essential process, the $Cu^+/(Cu^{2+}+Cu^+)$ ratio was determined by evaluating the relative area of the Cu^+ peak vis-à-vis the combined area of the Cu^+ and Cu^{2+} peaks. Importantly, the $Cu^+/(Cu^{2+}+Cu^+)$ ratio for $CuCeO_x$ surpass those of $CuZrO_x$, and $CuLaO_x$. This disparity indicates that the occurrence of these Cu^+ species at the interfaces of Cu-Ce, Cu-Zr, and Cu-La prompts surface oxygen vacancies, ultimately enhancing oxygen mobility during the toluene oxidation process. The $O_a/(O_L+O_a)$ ratio was determined by assessing the proportionate area of the O_a peak in relation to the total area of the O_L and O_a peaks. Notably, the $O_a/(O_L+O_a)$ ratios display minimal variation across the $CuCeO_x$, $CuZrO_x$, and $CuLaO_x$ catalysts, falling within the range of 0.53 to 0.63. In concordance with the Mars-van Krevelen reaction mechanism, wherein O_L primarily partakes in toluene oxidation, the dominance of O_L in the process is corroborated, surpassing the role of O_a. This outcome will be further corroborated through O_2-TPD analysis.

Temperature programmed thermal analysis

The H_2-TPR analysis, illustrated in Figure 3, elucidates the redox characteristics inherent in the $CuCeO_x$, $CuZrO_x$, and $CuLaO_x$ catalysts. The α reduction peak indicates the reduction of Cu-[O_x]-M species (M=Ce, Zr, La), resulting from the inclusion of copper ions into Ce, Zr, and La's surface lattice (Ayastuy et al. 2010 The β reduction peak signifies the reduction of dispersed CuO_x species on the catalyst surface (Chen et al. 2015). Similarly, the γ reduction peak corresponds to the reduction of bulk-phase copper oxide (Bin et al. 2014). Remarkably, the reduction process extends beyond the surface, penetrating into the catalyst's bulk. This profound bulk reduction can potentially expedite the reduction kinetics, leading to heightened hydrogen consumption. Of particular significance is the observed synergistic effect arising from Cu-Ce interactions, contributing to lower reduction temperatures when compared to Cu-Zr and Cu-La interactions. The findings in Table 2 underscore that $CuCeO_x$ exhibits greater H_2 consumption (2.90 mmol·g^{-1}) compared to $CuZrO_x$ (1.69 mmol·g^{-1}) and $CuLaO_x$ (0.67 mmol·g^{-1}). Notably, the reduction temperature associated with the α peak is markedly lower for $CuCeO_x$ (199°C) in contrast to $CuZrO_x$ (279°C) and $CuLaO_x$ (490°C). It is pertinent to underscore that the subsequent section will delve into the catalytic activity test, thereby validating the observed redox properties of the

Table 2. Redox properties of $CuCeO_x$, $CuZrO_x$ and $CuLaO_x$ catalysts detected by H_2-TPR.

	α peak		β peak		γ peak		
Catalyst	T (°C)	H_2 uptake (mmol·g^{-1})	T (°C)	H_2 uptake (mmol·g^{-1})	T (°C)	H_2 uptake (mmol·g^{-1})	Total uptake (mmol·g^{-1})
$CuCeO_x$	199	0.76	357	1.37	434	0.77	2.90
$CuZrO_x$	279	0.25	347	0.97	395	0.48	1.69
$CuLaO_x$	490	0.33	529	0.25	555	0.09	0.67

catalysts. Significantly, these properties exhibit a descending trend concerning their respective reduction temperatures, particularly focusing on the α peak temperature. This trend diverges from hydrogen consumption behavior and follows the sequence of $CuCeO_x$ > $CuZrO_x$ > $CuLaO_x$.

O_2-TPD analysis unveils valuable insights into the generation and mobility of oxygen species, as detailed in Figure 4 and Table 3. This investigation reveals the presence of two distinct oxygen species types across all catalysts: surface-adsorbed oxygen (O_a) and lattice oxygen (O_L). Surface-adsorbed oxygen, encompassing O_2^- and O_2^{2-}/O^-, manifests at temperatures below 450°C, arising from oxygen adsorption onto surface vacancies (Rao et al. 2022). For $CuCeO_x$, the O_2-TPD profile shows a desorption peak around 354°C, indicating the mild desorption of surface oxygen species. A noticeable peak appearing above 930°C is attributed to the desorption of lattice oxygen. For $CuZrO_x$, its pronounced thermal stability results in a slight lattice oxygen desorption peak at 634°C, without observable desorption of surface oxygen species. Conversely, $CuLaO_x$ exhibits a distinctive O_2-TPD profile characterized by two broad desorption peaks at 318°C and 691°C, respectively. Notably, these peaks demonstrate significantly larger areas compared to $CuCeO_x$ and $CuZrO_x$ (Table 3). The substantial desorption of surface oxygen species in $CuLaO_x$ suggests

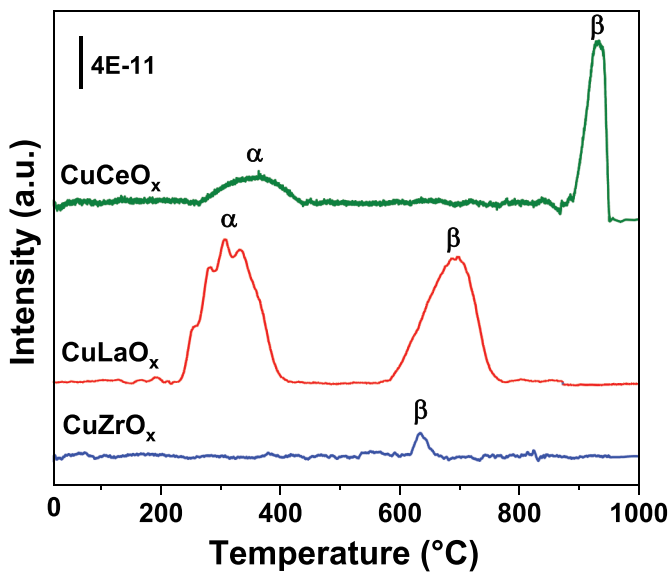

Figure 4. O_2-TPD profiles of $CuCeO_x$, $CuZrO_x$ and $CuLaO_x$ catalysts. Weight of catalyst: 20 mg; pretreatment: pure ar at 500°C for 30 min; measurement conditions: pre-adsorbed pure O_2 (30 mL/min), heating rate 10°C/min from 50–1000°C.

Table 3. Oxygen mobility of $CuCeO_x$, $CuZrO_x$ and $CuLaO_x$ catalysts detected by O_2-TPD.

	α peak		β peak		
Catalyst	T (°C)	O_2 desorption (umol·g^{-1})	T (°C)	O_2 desorption (umol·g^{-1})	Total desorption (umol·g^{-1})
$CuCeO_x$	356	22.0	932	40.1	62.1
$CuZrO_x$	/	/	633	5.39	5.4
$CuLaO_x$	312	96.6	693	80.3	176.9

that Cu-La interaction enhances oxygen mobility, fostering the production of surface oxygen vacancies, surpassing those observed in $CuCeO_x$ and $CuZrO_x$. Furthermore, the lattice oxygen in $CuLaO_x$ is more readily dissociated from the bulk than in $CuCeO_x$ and $CuZrO_x$, indicating the greater role of abundant lattice oxygen in the toluene oxidation process.

Catalytic activity testing

The catalytic performance of the synthesized $CuCeO_x$, $CuZrO_x$, and $CuLaO_x$ catalysts is clearly depicted in Figure 5a, spanning the temperature range of 25°C to 400°C. Across this temperature range, all catalysts exhibited a progressive enhancement in toluene conversion, reflecting successful toluene elimination. It's worth mentioning that among the evaluated catalysts, $CuLaO_x$ exhibited the most subdued catalytic activity, a characteristic ascribed to its relatively diminished reducibility at lower temperatures. Specifically, the performance profile of $CuLaO_x$ can be characterized by a gradual onset of catalytic activity starting at 50°C, which is followed by a relatively gradual and sustained reaction rate until reaching 325°C. After that, another step exhibits a fast reaction rate with temperature, leading to the toluene conversion from 29% (325°C) to 94% (400°C). The conversion of toluene using $CuZrO_x$ is indicated by an "S-shaped" curve, with toluene ignition occurring at around 175°C, attaining complete conversion at 325°C. Additionally, the $CuCeO_x$ catalyst illustrates a unique two-phase mechanism, corresponding to the temperature ranges of 150–200°C and 225–250°C, respectively. The rate for this catalyst at two step appears similar to those of the $CuZrO_x$ catalyst, reaching the 100% toluene conversion at 257°C. Indeed, $CuCeO_x$ demonstrates optimal redox properties at low temperatures (as observed in H_2-TPR), which accounts for the superior activity exhibited by this catalyst. The catalytic performance of pure CuO and CeO_2 was also obtained in Figure 1, and exhibit lower activity than that of $CuCeO_x$、$CuZrO_x$ and $CuLaO_x$. CO_2 yield (Y_{CO2}) was obtained in the form of the percentage of the produced CO_2 concentration at the exit (C_{pro}) and the total CO_2 content was calculated by the theoretical conversion rate of toluene (C_{total}) for all catalysts ($Y_{CO2} = C_{pro}/ C_{total}$), as shown in Figure 5b. CO_2 yield increased synchronously with toluene conversion, but such a profile lagged behind that of toluene conversion with temperature, particularly for the $CuCeO_x$. Namely, as the reaction temperature reached 200°C, the $CuCeO_x$ achieved a toluene conversion of 49.5%, exceeding the CO_2 yield of 13.4%. When the temperature was further increased to 250°C, the toluene conversion and CO_2 yield reached 93.1% and 15.2%, respectively. Decomposed toluene can be converted entirely into CO_2 and H_2O by using the $CuCeO_x$, $CuZrO_x$, and $CuLaO_x$ catalysts at temperatures of 298, 339, and 372°C, respectively. The by-products species was also considered and not detected over $CuCeO_x$ in the toluene oxidation process, as shown in Figure 2, which is

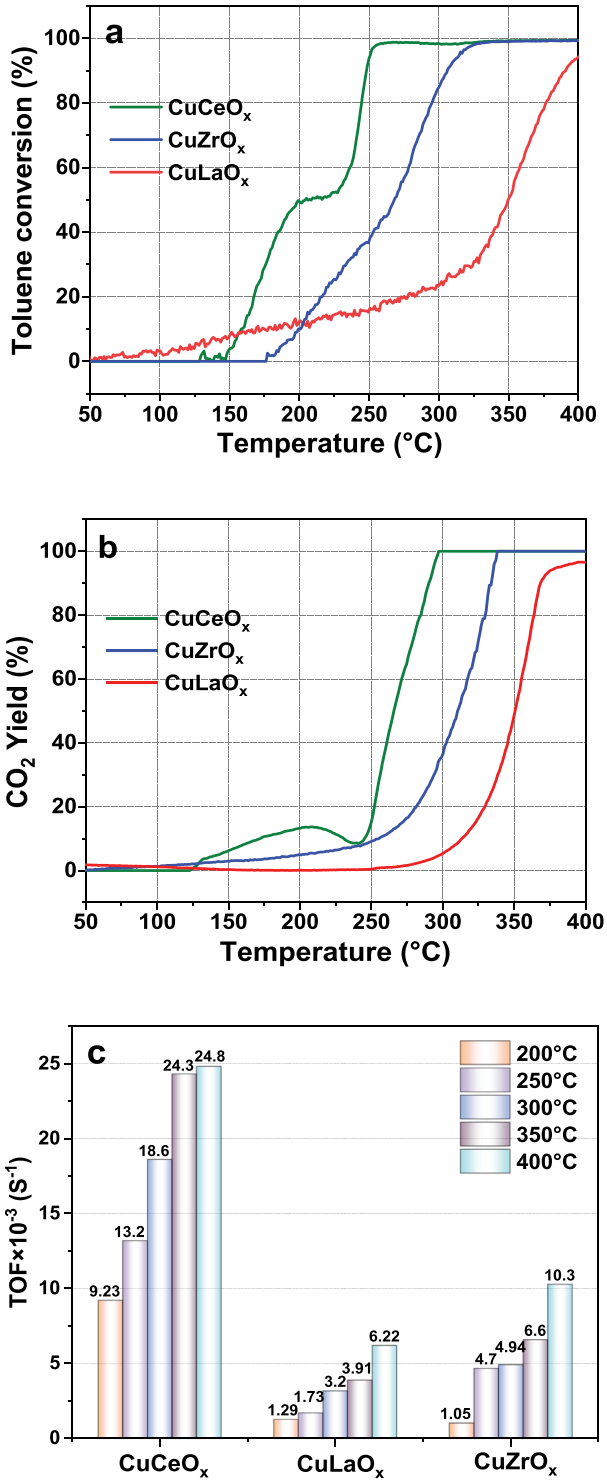

Figure 5. Toluene conversion (a), CO_2 yield (b) and TOF (c) as a function of the temperature of $CuCeO_x$, $CuZrO_x$ and $CuLaO_x$ catalysts. Conditions: 500 ppm toluene and air to balance (total 300 mL/min); weight of catalyst: 200 mg; heating rate: 5°C/min.

probably due to the relatively low reaction temperature. The turnover frequency (TOF) can be calculated according to the toluene conversion and copper species of the α peak in H_2-TPR, since the β and γ peaks are located at the temperature higher than 300°C, leading to a weak contribution to the toluene oxidation. And the TOF value of catalysts was also compared with other metal-based catalysts reported previously (Table S1). As shown in Figure 5c, TOF are $9.23–24.8 \times 10^{-3}$ s^{-1}, $1.29–6.22 \times 10^{-3}$ s^{-1}, and $1.05–10.03 \times 10^{-3}$ s^{-1} within the reaction temperature of 200–400°C for the $CuCeO_x$, $CuLaO_x$ and $CuZrO_x$ catalysts, respectively. The TOF increases steadily with temperature for all the tested catalysts. Comparatively, the $CuCeO_x$ catalyst exhibits a higher TOF than the $CuLaO_x$ and $CuZrO_x$ catalysts in the same temperature range, suggesting that the sensitivity of the toluene oxidation process is as follows: $CuCeO_x$ > $CuZrO_x$ > $CuLaO_x$.

In situ IR study and catalytic reaction mechanisms

A comprehensive investigation of the toluene oxidation reaction mechanism was undertaken through in situ infrared (IR) experiments conducted under ambient air conditions. The outcomes, as presented in Figure 6, illustrate the spectral responses at varying temperatures, both in the presence and absence of gaseous oxygen. Interestingly, despite distinctive catalyst compositions, a consistent reaction pathway was observed across all catalysts. In the context of a 500 ppm toluene + 21% O_2/Ar atmosphere, discernible bands emerged within the range of 3073–2883 cm^{-1}, attributed to the C-H stretching vibrations of the toluene aromatic ring (Moreno-Roman et al. 2023). Furthermore, spectral bands within the range of 1610–1300 cm^{-1} correlated with C=C stretching vibrations characteristic of aromatic rings (Li et al. 2020, affirming the adsorption of toluene molecules onto the catalyst surface while preserving the aromatic ring structure. Bands seen at 2934 and 2883 cm^{-1} were assigned to methylene (-CH_2) vibrations rather than methyl (-CH_3). This assignment is backed by their deviation from the typical methyl C-H stretching vibrations of methyl groups, which are generally observed between 2970–2950 cm^{-1} (Yan Yan et al. 2019). Bands with low intensity at 1075 and 1034 cm^{-1} were ascertained to be the stretching vibrations associated with alkoxide species (Jeong et al. 2013; Wang et al. 2022). These findings indicate that toluene, when adsorbed on the active copper sites of the catalyst surface, engages with either lattice oxygen species or active oxygen species adsorbed on the surface, which are produced due to oxygen vacancies in the catalyst (Dong et al. 2020, Mo et al. 2020. This interaction leads to the cleavage of the C-H bond within the methyl group, resulting in the formation of benzyl species (C_6H_5-CH_2), which are subsequently oxidized into alkoxide species. Additional bands at 2739 cm^{-1} are associated with typical aldehydic species, while bands at 1376 cm^{-1} (O-H) indicate the formation of carboxylic acid species. Higher reaction temperatures result in an augmented chemical adsorption of toluene, as indicated by the heightened intensity of bands within the 3073–2883 cm^{-1} range. Bands attributed to alkoxide, aldehydic, and carboxylic acid species (1610–1000 cm^{-1}) maintain consistent intensity across all temperatures up to 400°C, followed by a significant increase in CO_2 (2400–2300 cm^{-1}) and H_2O (4000–3500 cm^{-1}) bands, particularly for $CuCeO_x$. This underscores the dominance of alkoxide in the reaction, serving as intermediates between reactants, intermediates, and catalysts (Sedmak, Hočevar, and Levec 2004)IR experiments were also carried out under a 500 ppm C_7H_8/N_2 atmosphere (without gaseous oxygen involvement), as shown in Figure 3 in the supporting information, resulting in lower

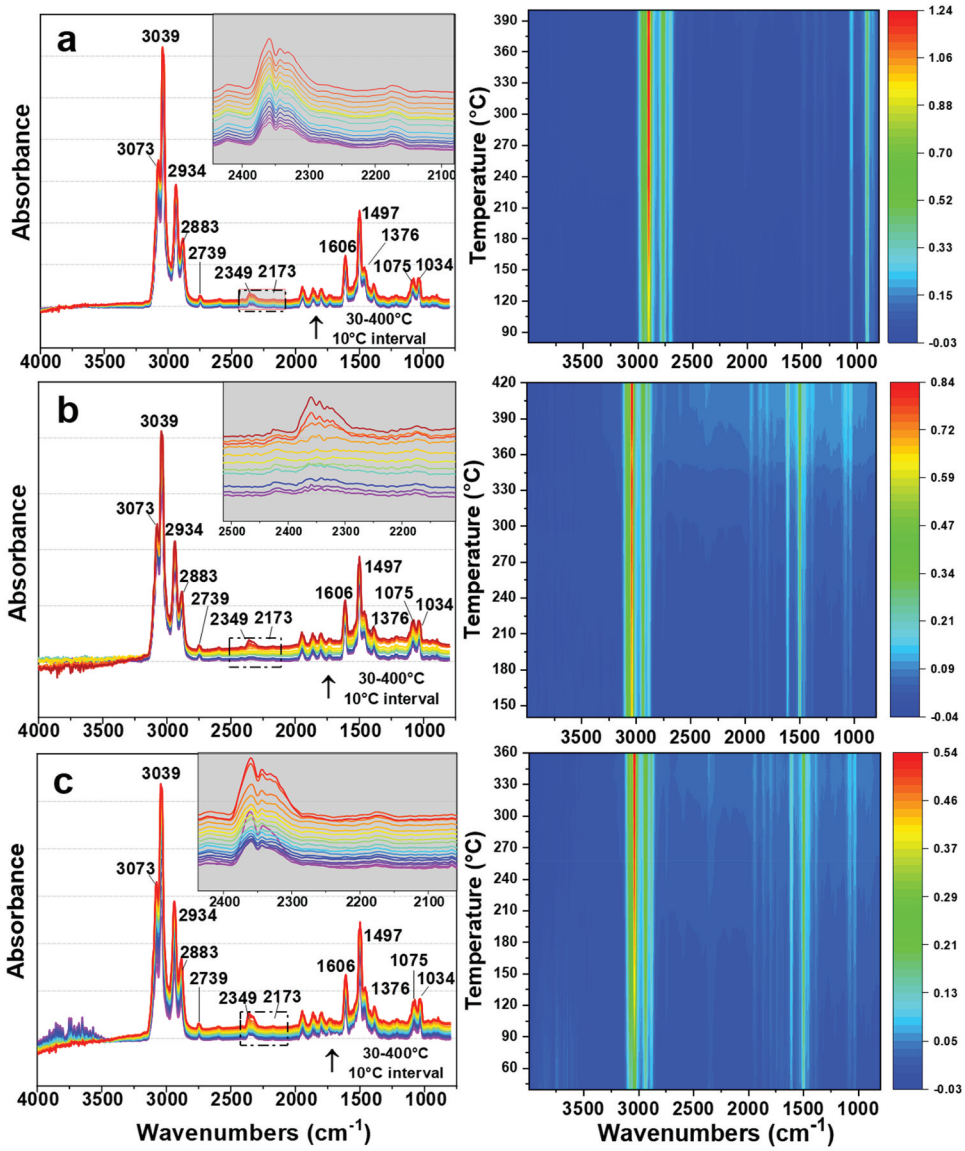

Figure 6. IR spectra of the oxidation of toluene over $CuCeO_x$ (a), $CuZrO_x$ (b) and $CuLaO_x$ (c) catalysts within the temperature range of 50–400°C. Conditions: 500 ppm toluene + 21% O_2/Ar (total flow rate: 500 mL/min); heating rate: 10°C/min.

intensities for alkoxide, aldehydic, and carboxylic acid species, as well as CO_2 and H_2O bands, compared to toluene oxidation with gaseous oxygen. This confirms the important function of reactive oxygen in enabling the opening of the ring of toluene. The collective evidence from activity tests and IR measurements suggests that toluene molecules initially adsorb at copper sites, interacting with both surface-adsorbed and lattice oxygen species on the catalyst surface. The involvement of lattice oxygen is crucial in the toluene oxidation process, leading to the creation of oxygen vacancies and various intermediates (including alkoxides, aldehydes, and carboxylic acid species). These intermediates are

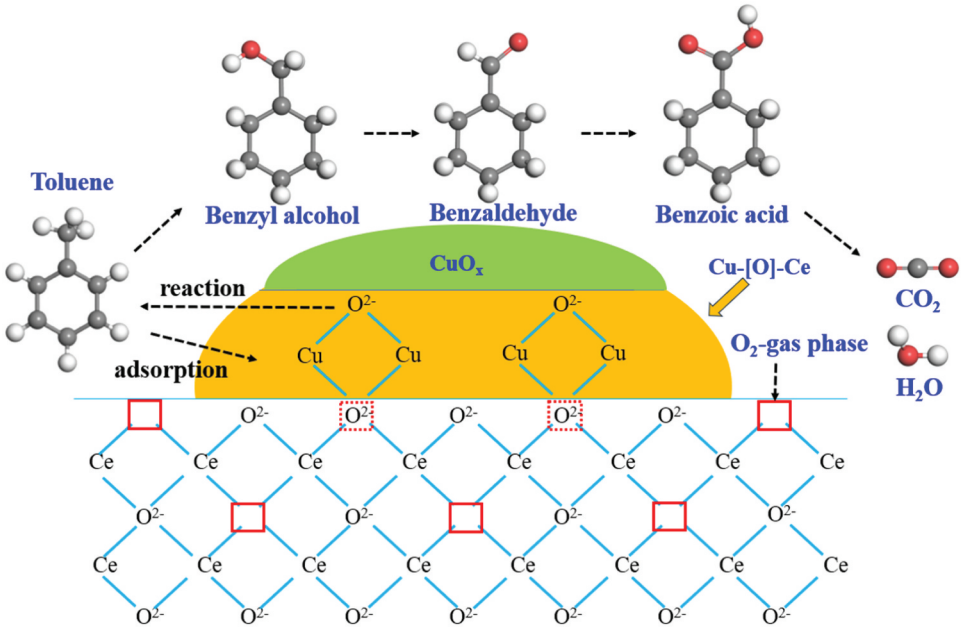

Figure 7. Reaction pathways of toluene oxidation over the $CuCeO_x$ catalyst.

gradually converted into CO_2 and H_2O through oxidation. Oxygen vacancies can be re-oxidized either by gas-phase oxygen or through bulk catalyst oxygen diffusion. Once another surface-active oxygen species is formed, toluene can be readmitted and engage with the active oxygen atoms, perpetuating the catalytic process. Among the evaluated catalysts, $CuCeO_x$ stands out due to its abundant lattice oxygen and reactive oxygen species, which expedite toluene oxidation. The process of toluene oxidation over $CuCeO_x$ catalysts generally occurs according to the Mars-van Krevelen mechanism, as shown in Figure 7.

Conclusions

The synthesis of $CuLaO_x$, $CuCeO_x$, and $CuZrO_x$ catalysts involved the utilization of nitrate precursors, followed by a comprehensive assessment of the impact of rare-earth promoters La_2O_3, CeO_2, and ZrO_2 on the physicochemical characteristics of these mixed oxides. Following this, the catalytic efficiency of these materials was evaluated in terms of toluene oxidation and conversion. The results showed that the inclusion of Ce, Zr, and La promoters enhanced the dispersion of copper oxides. In the instance of $CuLaO_x$, a profusion of surface oxygen species was evident, with no discernible CuO crystalline phase detected. Despite ZrO_2 functioning as a support in amorphous form, the CuO particle sizes reached 7.1 nm, as indicated by XRD results. Regarding $CuCeO_x$, the incorporation of Ce enhanced the reducibility of copper species, as evident from H_2-TPR results. The Cu-Ce interaction, as demonstrated by O_2-TPD results, notably boosted the catalytic activity during toluene oxidation. Consequently, the turnover frequencies (TOF) for $CuCeO_x$, $CuLaO_x$, and $CuZrO_x$ catalysts were determined as $9.23–24.8 \times 10^{-3}$ s^{-1}, $1.29–6.22 \times 10^{-3}$ s^{-1}, and $1.05–10.03 \times 10^{-3}$ s^{-1} within the temperature range of 200–400°C. Infrared (IR) experiments

provided complementary evidence regarding the involvement of both adsorbed oxygen and lattice oxygen species in the toluene oxidation mechanism. Notably, a variety of intermediates were observed, and they underwent comprehensive oxidation to yield CO_2 and H_2O, all without the need for external gaseous oxygen replenishment. The catalytic oxidation process appeared to proceed through the sequence of toluene-alkoxide-aldehydic-carboxylic acid intermediates, culminating in complete degradation into CO_2 and H_2O.

Disclosure statement

No potential conflict of interest was reported by the author(s).

Funding

This work was supported by YLU-DNL Fund (2021004), Key R&D Program of ShaanXi Province (2023-YBSF-442), National Natural Science Foundation of China (52106275).

Data availability statement

Data will be made available on request.

Credit authorship contribution statement

Guangtao Hu: Design, Methodology, Data curation, Formal analysis, Investigation, Funding acquisition, Writing-original draft, Writing-review & editing. **Zirui Zhang**: Formal analysis, Methodology. **Chang'an Wang**: Formal analysis, Results discussion. **Guojie Li**: Formal analysis, Results discussion. **Dandan Zhou**: Formal analysis, Results discussion. **Jinshi Wang**: Formal analysis, Methodology. **Defu Che**: Investigation, Writing-review & editing, Supervision, Funding acquisition, Project administration. **Running Kang**: Design, Methodology, Results discussion, Writing-review & editing.

References

Aasberg-Petersen, K., I. Dybkjær, C. V. Ovesen, N. C. Schjødt, J. Sehested, and S. G. Thomsen. 2011. Natural gas to synthesis gas-catalysts and catalytic processes. *J. Nat. Gas. Sci. Eng* 3:423–59. doi:10.1016/j.jngse.2011.03.004.

Arandiyan, H., Y. Peng, C. Liu, H. Chang, and J. Li. 2014. Effects of noble metals doped on mesoporous LaAlNi mixed oxide catalyst and identification of carbon deposit for reforming CH_4 with CO_2. *J. Chem. Technol. Biotechnol.* 89:372–81. doi:10.1002/jctb.4127.

Ayastuy, J. L., A. Gurbani, M. P. Gonzalez-Marcos, and M. A. Gutiérrez-Ortiz. 2010. Effect of copper loading on copper-ceria catalysts performance in CO selective oxidation for fuel cell applications. *Int. J. Hydrogen Energ* 35:1232. doi:10.1016/j.ijhydene.2009.11.098.

Bin, F., C. Song, G. Lv, J. Song, S. Wu, and X. Li. 2014. Selective catalytic reduction of nitric oxide with ammonia over zirconium-doped copper/ZSM-5 catalysts. *Appl. Catal. B Environ.* 150–151:532–43. doi:10.1016/j.apcatb.2013.12.052.

Bin, F., X. Wei, B. Li, and K. S. Hui. 2015. Self-sustained combustion of carbon monoxide promoted by the cu-Ce/ZSM-5 catalyst in $CO/O_2/N_2$ atmosphere. *Appl. Catal. B Environ.* 162:282–88. doi:10.1016/j.apcatb.2014.07.007.

Boycheva, S., D. Zgureva, M. Václavíkovác, Y. Kalvachev, H. Lazarova, and M. Popovae. 2019. Studies on non-modified and copper-modified coal ash zeolites as heterogeneous catalysts for VOCs oxidation. *J. Hazard. Mater* 361:374–82. doi:10.1016/j.jhazmat.2018.07.020.

Brummer, V., S. Y. Teng, D. Jecha, P. Skryja, V. Vavrcikova, and P. Stehlik. 2022. Contribution to cleaner production from the point of view of VOC emissions abatement: A review. *J. Clean. Prod.* 361:132112. doi:10.1016/j.jclepro.2022.132112.

Chen, G., Q. Xu, Y. Yang, C. Li, T. Huang, G. Sun, S. Zhang, D. Ma, and X. Li. 2015. Facile and mild strategy to construct mesoporous CeO_2–CuO nanorods with enhanced catalytic activity toward CO oxidation. *ACS Appl. Mater. Interfaces* 7 (42):23538. doi:10.1021/acsami.5b06495.

Cheng, Z., Q. Wu, J. Li, and Q. Zhu. 1996. Effects of promoters and preparation procedures on reforming of methane with carbon dioxide over Ni/Al_2O_3 catalyst. *Catal. Today* 30:147–55. doi:10.1016/0920-5861(95)00005-4.

Deng, H., Y. Lu, T. Pan, L. Wang, C. Zhang, and H. He. 2023. Metals incorporated into OMS-2 lattice create flexible catalysts with highly efficient activity in VOCs combustion. *Appl. Catal B Environ.* 320:121955. doi:10.1016/j.apcatb.2022.121955.

Dong, C., Z. Qu, X. Jiang, and Y. Ren. 2020. Tuning oxygen vacancy concentration of MnO_2 through metal doping for improved toluene oxidation. *J. Hazard. Mater* 391:122181. doi:10.1016/j.jhazmat.2020.122181.

Doukkali, M. E., A. Iriondo, P. L. Arias, J. F. Cambra, I. Gandarias, and V. L. Barrio. 2012. Bioethanol/Glycerol mixture steam reforming over pt and PtNi supported on lanthana or ceria doped alumina catalysts. *Int. J. Hydrog Energy* 37 (10):8298–309. doi:10.1016/j.ijhydene.2012.02.154.

Dudric, R., A. Vladescu, V. Rednic, M. Neumann, I. G. Deac, and R. Tetean. 2014. XPS study on $La_{0.67}Ca_{0.33}Mn_{1-x}Co_xO_3$ compounds. *J. Mol. Struct* 1073:66–70. doi:10.1016/j.molstruc.2014.04.065.

Gao, R., X. Tian, X. Ding, Z. Hou, Z. Li, X. Yu, J. Wang, L. Wu, L. Jing, J. Deng, et al. 2023. Regulating catalytic stability of PtSnM/CeO_2 (M = mn, W, nb) catalysts via the closely coupled multi-active sites to promote multicomponent VOCs oxidation. *Chem. Engine. J* 471:144456. doi:10.1016/j.cej.2023.144456.

Guo, M., K. Lia, L. Liu, H. Zhang, W. Guo, X. Hua, X. Meng, J. Jia, and T. Sun. 2019. Manganese-based multi-oxide derived from spent ternary lithium-ions batteries as high-efficient catalyst for VOCs oxidation. *J. Hazard. Mater* 380:120905. doi:10.1016/j.jhazmat.2019.120905.

Hong, J., W. Chu, P. A. Chernavskii, and A. Y. Khodakov. 2010. Effects of zirconia promotion on the structure and performance of smaller and larger pore silica-supported cobalt catalysts for Fischer–tropsch synthesis. *Appl. Catal. A Gen* 382 (1):28–35. doi:10.1016/j.apcata.2010.04.010.

Hu, J., W. B. Li, and R. F. Liu. 2018. Highly efficient copper-doped manganese oxide nanorod catalysts derived from CuMnO hierarchical nanowire for catalytic combustion of VOCs. *Catal. Today* 314:147–53. doi:10.1016/j.cattod.2018.02.009.

Jeong, M. G., E. J. Park, H. O. Seo, K. D. Kim, Y. D. Kim, and D. C. Lim. 2013. Humidity effect on photocatalytic activity of TiO_2 and regeneration of deactivated photocatalysts. *Appl. Surf. Sci.* 271:164–70. doi:10.1016/j.apsusc.2013.01.155.

Jones, S. D., L. M. Neal, M. L. Everett, G. B. Hoflund, and H. E. Hagelin-Weaver. 2010. Characterization of ZrO_2-promoted Cu/ZnO/nano-Al_2O_3 methanol steam reforming catalysts. *Appl. Sur. Sci* 256:7345–53. doi:10.1016/j.apsusc.2010.05.021.

Kanchana, S. K., N. Vanitha, R. B. Basavaraj, and M. Shivaraj. 2023. Structural and optical properties of polyvinyl alcohol/copper oxide (Pva/cuo) nanocomposites. *Solid. State Commun* 370:115221. doi:10.1016/j.ssc.2023.115221.

Kang, R., P. Ma, J. He, H. Li, F. Bin, X. Wei, B. Dou, K. N. Hui, and K. S. Hui. 2021. Transient behavior and reaction mechanism of CO catalytic ignition over a CuO–CeO_2 mixed oxide. *Proc. Combust. Inst* 38 (4):6493–501. doi:10.1016/j.proci.2020.06.186.

Li, R., L. Guo, S. F. S. Zhu, S. Dong, X. Ida, L. Zhang, L. Zhang, and L. Guo. 2020. Layered δ-MnO_2 as an active catalyst for toluene catalytic combustion. *Appl. Catal A: General* 602:117715. doi:10.1016/j.apcata.2020.117715.

Liu, L., J. Jia, T. Sun, and H. Zhang. 2018. A facile method for scalable preparation of mesoporous structured $SmMnO_3$ perovskites sheets for efficient catalytic oxidation of toluene. *Mater. Lett.* 212:107–10. doi:10.1016/j.matlet.2017.10.048.

Liu, Q., J. Mi, X. Chen, S. Wang, J. Chen, and J. Li. 2021. Effects of phosphorus modification on the catalytic properties and performance of CuCeZr mixed metal catalyst for simultaneous removal of CO and NO_x. *Chem. Engine. J* 423:130228. doi:10.1016/j.cej.2021.130228.

Mo, S., Q. Zhang, J. Li, Y. Sun, Q. Ren, S. Zou, Q. Zhang, J. Lu, M. Fu, D. Mo, et al. 2020. Highly efficient mesoporous MnO_2 catalysts for the total toluene oxidation: Oxygen-vacancy defect engineering and involved intermediates using in situ DRIFTS. *Appl. Catal. B Environ.* 264:118464. doi:10.1016/j.apcatb.2019.118464.

Moreno-Roman, E. J., J. González-Cobos, N. Guilhaume, and S. Gil. 2023. Toluene and 2-propanol mixture oxidation over Mn_2O_3 catalysts: Study of inhibition/promotion effects by in-situ DRIFTS. *Chem. Engine. J* 470:144114. doi:10.1016/j.cej.2023.144114.

Mu, S., D. Li, B. Hou, L. Jia, J. Chen, and Y. Sun. 2010. Influence of ZrO_2 loading on SBA-15-Supported cobalt catalysts for Fischer–Tropsch synthesis. *Energy Fuels* 24 (7):3715–18. doi:10.1021/ef901274y.

Mu, Z., J. J. Li, H. Tian, Z. P. Hao, and S. Z. Qiao. 2008. Synthesis of mesoporous Co/Ce-SBA-15 materials and their catalytic performance in the catalytic oxidation of benzene. *Mater. Res. Bull* 43 (10):2599–606. doi:10.1016/j.materresbull.2007.10.037.

Paul, A., A. R. Silva, M. M. A. Soliman, J. Karačić, B. Šljukić, E. C. B. A. Alegria, R. A. Khan, M. F. C. Guedes da Silva, and A. J. L. Pombeiro. 2022. Benzimidazole Schiff base copper (II) complexes as catalysts for environmental and energy applications: VOC oxidation, oxygen reduction and water splitting reactions. *Int. J. Hydrog. Energy* 47:23175–90. doi:10.1016/j.ijhydene.2022.04.271.

Piumetti, M., D. Fino, and N. Russo. 2015. Mesoporous manganese oxides prepared by solution combustion synthesis as catalysts for the total oxidation of VOCs. *App. Catal. B: Environ* 163:277–87. doi:10.1016/j.apcatb.2014.08.012.

Qiang, W., Q. Huang, J. Shen, Q. Ke, J. Lü, and Y. Guo. 2022. Copper oxide and manganese dioxide nanoparticles on corrugated glass-fiber supporters promote thermocatalytic oxidation of formaldehyde. *J. Clean. Pro* 368:133089. doi:10.1016/j.jclepro.2022.133089.

Rao, Y., Y. Zhang, J. Fan, G. Wei, D. Wang, F. Han, Y. Huang, and J. Croue. 2022. Enhanced peroxymonosulfate activation by Cu-doped $LaFeO_3$ with rich oxygen vacancies: Compound-specific mechanisms. *Chem. Engine. J* 435:134882. doi:10.1016/j.cej.2022.134882.

Reddy, B. M., L. Katta, and G. Thrimurthulu. 2010. Reply to comment on "novel nanocrystalline $Ce_{1-x}La_xO_{4r}$ (x = 0.2) solid solutions: Structural characteristics and catalytic performance". *Chem. Mater* 22:467–75. doi:10.1021/cm903282w.

Sedmak, G., S. Hočevar, and J. Levec. 2004. Transient kinetic model of CO oxidation over a nanostructured $Cu_{0.1}Ce_{0.9}O_{2-y}$ catalyst. *J. Catal* 222:87–99. doi:10.1016/j.jcat.2003.10.006.

Sepehri, S., and M. Rezaei. 2015. Preparation of highly active nickel catalysts supported on mesoporous nanocrystalline γ-Al_2O_3 for methane autothermal reforming. *Chem. Eng. Technol.* 38 (9):1637–45. doi:10.1002/ceat.201400566.

Srinivas, D., C. Satyanarayana, H. Potdar, and P. Ratnasamy. 2003. Structural studies on NiO-CeO_2-ZrO_2 catalysts for steam reforming of ethanol. *Appl. Catal A Gen* 246 (2):323–34. doi:10.1016/S0926-860X(03)00085-1.

Tsoncheva, T., G. Issaa, T. Blasco, M. Dimitrov, M. Popova, S. Hernández, D. Kovacheva, G. Atanasova, and J. M. L. Nieto. 2013. Catalytic VOCs elimination over copper and cerium oxide modified mesoporous SBA-15 silica. *Appl. Catal A Gen* 453:1–12. doi:10.1016/j.apcata.2012.12.007.

Vizcaíno, A. J., A. Carrero, and J. A. Calles. 2012. *Hydrogen production: Prospects and processes*, 247–94. New York: Nova Science Publishers, Inc.

Wang, B. Y., Y. X. Liu, J. J. Weng, P. Glarborg, and Z. Y. Tian. 2017. New insights in the low-temperature oxidation of acetylene. *Proc. Combust. Inst* 36 (1):355–63. doi:10.1016/j.proci.2016.06.163.

Wang, L. C., Q. Liu, M. Chen, Y. M. Liu, Y. Cao, H. Y. He, and K. N. Fan. 2007. Structural evolution and Catalytic Properties of nanostructured Cu/ZrO_2 catalysts prepared by oxalate gel-coprecipitation technique. *J. Phy. Chem. C* 111:16549–57. doi:10.1021/jp075930k.

Wang, P., J. Wang, J. Zhao, X. Ma, X. Du, S. Peng, X. Hao, B. Tang, A. Abudula, and G. Guan. 2022. Trace holmium assisting delaminated OMS-2 catalysts for total toluene oxidation at low temperature. *J. Colloid Interface Sci.* 608:1662–75. doi:10.1016/j.jcis.2021.10.077.

Wang, X., K. Huang, L. Yuan, S. Xi, W. Yan, Z. Geng, Y. Cong, Y. Sun, H. Tan, X. Wu, et al. 2018. Activation of surface oxygen sites in a cobalt-based perovskite model catalyst for CO oxidation. *J. Phys. Chem. Lett.* 9:4146–454. doi:10.1021/acs.jpclett.8b01623.

Yan, N., Q. Hao, C. Zhao, D. Yang, B. Dou, K. S. Hui, and K. N. Hui. 2019. Studies on $CuCe_{0.75}Zr_{0.25}O_x$ preparation using bacterial cellulose and its application in toluene complete oxidation. *Chem. Select* 4:4355–63. doi:10.1002/slct.201900727.

Ye, Y., J. Xu, L. Gao, S. Zang, L. Chen, L. Wang, and L. Mo. 2023. CuO/CeO_2 catalysts prepared by modified impregnation method for ethyl acetate oxidation. *Chem. Engine. J* 471:144667. doi:10.1016/j.cej.2023.144667.

Yun, J. Y., L. K. Wu, Q. L. Hao, Z. H. Teng, X. Gao, B. J. Dou, and F. Bin. 2022. Non-equilibrium plasma enhanced oxygen vacancies of CuO/CeO_2 nanorod catalysts for toluene oxidation. *J. Environ. Chem. Eng.* 10:107847. doi:10.1016/j.jece.2022.107847.

Zhang, C., S. Li, M. Li, S. Wang, X. Ma, and J. Gong. 2012. Enhanced oxygen mobility and reactivity for ethanol steam reforming. *AICHE J.* 58:516–25. doi:10.1002/aic.12599.

Zhang, Z., G. Hu, C. Zhao, X. Wei, B. Dou, W. Liang, and F. Bin. 2023. Insights into the reaction mechanism of toluene oxidation by isotope dynamic experiment and the kinetics over MCeZr/TiO_2 (M = cu, mn, ni, co and fe) catalysts. *Fuel* 341:127760. doi:10.1016/j.fuel.2023.127760.

Zhao, C., Q. Hao, Q. Zhang, N. Yan, J. Liu, B. Dou, and F. Bin. 2019. Catalytic self-sustained combustion of toluene and reaction pathway over $Cu_xMn_{1-x}Ce_{0.75}Zr_{0.25}/TiO_2$ catalysts. *Appl. Catal A Gen* 569:66–74. doi:10.1016/j.apcata.2018.10.034.